



**HAL**  
open science

## Rapid microwave synthesis of magnetic nanoparticles in physiological serum

Thomas Girardet, Lyns Verel Che Dji, Sabine Bouguet-Bonnet, Franck Cleymand, Solenne Fleutot

► **To cite this version:**

Thomas Girardet, Lyns Verel Che Dji, Sabine Bouguet-Bonnet, Franck Cleymand, Solenne Fleutot. Rapid microwave synthesis of magnetic nanoparticles in physiological serum. *Pure and Applied Chemistry*, 2022, 10.1515/pac-2022-0601 . hal-03782794

**HAL Id: hal-03782794**

**<https://hal.science/hal-03782794v1>**

Submitted on 21 Sep 2022

**HAL** is a multi-disciplinary open access archive for the deposit and dissemination of scientific research documents, whether they are published or not. The documents may come from teaching and research institutions in France or abroad, or from public or private research centers.

L'archive ouverte pluridisciplinaire **HAL**, est destinée au dépôt et à la diffusion de documents scientifiques de niveau recherche, publiés ou non, émanant des établissements d'enseignement et de recherche français ou étrangers, des laboratoires publics ou privés.

# Rapid microwave synthesis of magnetic nanoparticles in physiological serum

Thomas Girardet, Lyns Verel Che Dji, Sabine Bouguet-Bonnet, Franck Cleymand, Solenne Fleutot\*

\*Corresponding author: Solenne Fleutot, Institut Jean Lamour, CNRS, Université de Lorraine, F-54000 Nancy, France, e-mail: solenne.fleutot@univ-lorraine.fr

Thomas Girardet, Franck Cleymand and Solenne Fleutot, Institut Jean Lamour, CNRS, Université de Lorraine, F-54000 Nancy, France

Lyns Verel Che Dji and Sabine Bouguet-Bonnet, CRM2, Université de Lorraine, F-54000 Nancy, France

Abstract:

Superparamagnetic Iron Oxide Nanoparticles (SPIONs) are more and more used in biomedical applications such as therapy (treatment for certain cancers, hyperthermia), diagnostic (contrast agent for Magnetic Resonance Imaging) or both. For these applications, SPIONs must be stable in an aqueous solution, monodisperse, with a narrow size distribution and without aggregation. To obtain these nanoparticles, a microwave process is carried out in this study as an easy, fast and reproducible synthesis method. Currently, in the literature, most synthesis of SPIONs are in ultra-pure water or another solvent. To consider the use of SPIONs in biomedical applications, it is essential to ensure the preservation of the physico-chemical parameters of the nanoparticles in the physiological medium to validate a synthesis process. With this objective, this study reports a comparison between the SPIONs synthesis in ultra-pure water and the SPIONs direct synthesis in a physiological serum (containing NaCl). To complete this comparison, the dispersion of SPIONs in physiological serum after an elaboration in ultra-pure water is reported. Characterizations of these different SPIONs samples are carried out to determine the physico-chemical parameters and magnetic properties. SPIONs are characterized by Transmission Electronic Microscopy, Dynamic Light Scattering, X-Ray Diffraction, Raman spectroscopy and magnetic measurements. Finally, to check if SPIONs can be used as contrast agent for MRI, a relaxometry measurement is performed.

Keywords: iron oxide nanoparticles; microwave process; contrast agent; physiological serum; NMR relaxometry.

## 1 Introduction

For several decades, nanoparticles (NPs) have been used in different fields such as energy storage [1], depollution [2], biomedical applications [3–6]. Indeed, thanks to their size between 1 to 100 nm, comparable to the size of cells, viruses, proteins, interaction between them allows to a great potential for these applications [7]. NPs are indeed used for applications in diagnostic (for example, as a contrast agent CA [8,9]), in therapy (hyperthermia [10,11]) or both (for example, with a drug delivery to treat cancer [12,13]) but the composition of these NPs can be different and adapted according to the targeted application. For example, silver NPs are used as antibacterial agents [14], magnetic NPs such as iron oxide or gadolinium complexes are used as CA [5,9,15].

CA allow to enhance image contrast and also to decrease the analysis time in MRI (Magnetic Resonance Imaging). The first CAs were developed during the 60s by Gramiak and Shah [16]. Then, during the 80s, several commercial CAs have been developed with a gadolinium core. Indeed, thanks to the magnetic behaviour of gadolinium  $Gd^{3+}$  (paramagnetism), the longitudinal relaxation time  $T_1$  decreases and the image contrast is improved. However,  $Gd^{3+}$  is neurotoxic: an organic layer around the inorganic core is mandatory to avoid a neurocellular destruction [17]. Superparamagnetic NPs are used to shorten the transverse relaxation time  $T_2$ .

Superparamagnetic Iron Oxide Nanoparticles (SPIONs) such as magnetite ( $Fe_3O_4$ ) or its oxidized form maghemite ( $\gamma-Fe_2O_3$ ) are commonly used as CA [5,9,13,18–21]. Indeed, SPIONs are biocompatible and different synthesis are well known. To use SPIONs as CA, NPs must be in an aqueous solution, with a narrow size distribution, with a good crystallinity and good magnetic properties. The different synthesis of SPIONs allow to obtain a part of these properties. For

example, the coprecipitation is a synthesis directly in an aqueous media with soft conditions but with a possible aggregation of NPs and a large size distribution [22–24]. To decrease this phenomena, an addition of a ligand during the synthesis can be used: different ligands have been added like for example citric acid [25–27], polyvinyl alcohol (PVA) [28], oleic acid [29], ethylene glycol [30].

Other synthesis allow to obtain SPIONs directly in water, such as hydrothermal synthesis [31] or microemulsion [32] but the conditions are hard and don't allow to obtain monodisperse NPs. The thermal decomposition is an alternative to synthesize SPIONs and presents the advantage of obtaining SPIONs which are monodisperse, with a narrow size distribution and a good crystallinity [33,34]. By thermal decomposition at high temperature, synthesized SPIONs are stable in an organic solution (cyclohexane, chloroform, toluene, ...), but a subsequent phase transfer step is therefore mandatory to use SPIONs for the biomedical applications [35,36].

To obtain monodisperse SPIONs in an aqueous media, a new synthesis is more and more used: the microwave synthesis [27,37–39]. Indeed, thanks to the microwave irradiations, the temperature is better controlled inside the reactor: there is a vibration of the solvent molecules generating local heating of the solution. Synthesized SPIONs are stable in an aqueous solution, monodisperse (because a ligand was added during the synthesis), with a good crystallinity and good magnetic properties.

Numerous studies describe the potential use of SPIONs but generally synthesized in ultra-pure water or dispersed in water after a phase transfer. However, in a living organism, there are several proteins and molecules which can lead to an aggregation of these NPs. To limit this phenomenon, we consider it important to obtain SPIONs that are stable in a physiological medium before application.

The goal of this study is to compare the synthesis of SPIONs in different aqueous media. Indeed, we compare a synthesis in ultra-pure water to a synthesis in physiological serum and to a redispersion of SPIONs in a physiological serum. For each synthesis, systematic characterizations are realized to determine the size, the crystallinity, the composition and the magnetic properties. Then, a comparison of relaxivity values of these different synthesis is performed to verify the influence of the physiological serum on the synthesis.

## 2 Experimental

### 2.1 Materials

Ferrous chloride ( $\text{FeCl}_2 \cdot 4\text{H}_2\text{O}$ ) and ferric chloride ( $\text{FeCl}_3 \cdot 6\text{H}_2\text{O}$ ) were purchased from Alfa Aesar. Citric acid ( $\text{C}_6\text{H}_8\text{O}_7$ ) and ammonium hydroxide solution ( $\text{NH}_4\text{OH}$ ) were purchased from Sigma Aldrich. For the experiments, ultrapure water (resistivity =  $18.2 \text{ M}\Omega \cdot \text{cm}$ ) or commercial physiological serum (with 0.9 g of NaCl per 100 mL of ultra-pure water) were used.

### 2.2 Synthesis

A previous work describes the synthesis used for this study [27]. A mixture of ferric chloride ( $\text{FeCl}_3 \cdot 6\text{H}_2\text{O}$ ; 3.70 mmol) and ferrous chloride ( $\text{FeCl}_2 \cdot 4\text{H}_2\text{O}$ ; 5.03 mmol) with citric acid ( $\text{C}_6\text{H}_8\text{O}_7$ ; 3.16 mmol) are solubilized in 15 mL of ultra-pure water or physiological serum in a Pyrex reactor for the microwave. This solution is stirred until homogenization. Then, 5 mL of ammonium hydroxide solution is added to the mixture to precipitate the solution. The solution turns black and is stirred again before being placed in the microwave to heat at  $96^\circ\text{C}$  for 40 min. A single-mode microwave (Monowave 400 from Anton Paar) is used. The system operates at a frequency of 2.45 GHz. The maximum power of this microwave is 850 W. The temperature is controlled by an external infrared sensor [40].

After heating, the solution is collected and washed by centrifugation for a purification step. The solution is centrifuged a first time with ethanol at 10 000 rpm for 5 min and a second time with a mixture of ultrapure water or physiological serum and ethanol at 10 000 rpm for 5 min. The nanoparticles (SPIONs) obtained are then dispersed in ultrapure water or physiological serum. A part is evaporated at  $60^\circ\text{C}$  to obtain powder for X-Ray Diffraction, Raman spectroscopy and magnetic measurements. The other part is kept in solution for Transmission Electronic Microscopy, Dynamic Light Scattering measurements and relaxometry measurements.

The obtained sample by the synthesis, the purification and the redispersion of iron oxide nanoparticles in ultra-pure water is named  $\text{NPs}_{\text{ww}}$ . The obtained sample by the synthesis and the purification in ultra-pure water then the redispersion in physiological serum is named  $\text{NPs}_{\text{wp}}$ . Finally, the obtained sample by the synthesis, the purification and the redispersion in physiological serum is named  $\text{NPs}_{\text{pp}}$ .

## 2.3 Characterization

Different techniques are used for the characterization of nanoparticles.

### 2.3.1 Transmission Electron Microscopy

Transmission Electron Microscopy (TEM) is used to determine the shape, the size and the solvent dispersion of nanoparticles. The TEM is a CM200-FEI operating at 200 kV (point resolution 0.27 nm) from Philips. The distribution of size is obtained using free software ImageJ [41].

### 2.3.2 Dynamic Light Scattering

Dynamic Light Scattering experiments (DLS) were performed by the ZETASIZER Nano ZS device from Malvern Instrumental. The aqueous solution of nanoparticles is diluted (final concentration of 0.2 mg/mL) to determine the hydrodynamic size distribution. The DLS measurements are performed three times and the average of these three measurements will be presented in this work.

### 2.3.3 X-Ray diffraction

X-Ray Diffraction (XRD) patterns were recorded in standard conditions with an INEL CPS120 equipped with a monochromatic cobalt radiation ( $\text{Co K}\alpha = 0.17886 \text{ nm}$ ) at grazing angle of incidence simultaneously on  $120^\circ$ . Crystallite size was calculated with the Debye-Scherrer equation from the most intense peak for (311) plane.

### 2.3.4 Raman spectroscopy

Raman scattering measurements were performed at room temperature with a laser at 633 nm. The scattered light is analysed by a monochromator with a 1800 lines/mm grating and with a Charge-Coupled Device (CCD) detector.

### 2.3.5 Magnetic measurements

The NPs magnetic properties in powder state were determined by Superconducting Quantum Interference Device (SQUID) with a Vibrating Sample Magnetometer (VSM) Quantum Design head. The saturation magnetization ( $M_s$ ) and the blocking temperature ( $T_B$ ) are the most important information obtained with this technique. The magnetization was measured by sweeping the magnetic field from +50 000 Oe (1 T = 10 000 Oe) to -50 000 Oe and then from -50 000 Oe to +50 000 Oe.

Magnetization curves as a function of the temperature were recorded as follows: samples were introduced in the SQUID at room temperature (300K) and cooled down to 5 K with no applied field after applying a careful degaussing procedure. A magnetic field of 200 Oe was then applied, and the magnetization was recorded upon heating from 5 to

300 K (Zero Field Cooled curves called ZFC curves). The sample was then cooled down to 5 K under the same applied field, and the magnetization was recorded upon heating from 5 to 300 K (Field Cooled curve called FC curves).

### 2.3.6 Relaxometry measurements

The longitudinal ( $R_1 = 1/T_1$ ) and transversal ( $R_2 = 1/T_2$ ) proton relaxation rates of water in solutions containing SPI-ONs at different concentrations were measured at 37°C and at 1.41T. The proton Larmor frequency corresponding to this magnetic field value is 60MHz and measurements were made with a Bruker Minispec MQ60.  $T_1$  values were measured with an inversion-recovery pulse sequence and  $T_2$  with a CPMG (Carr-Purcell-Meiboom-Gill) pulse sequence. The relaxivities (longitudinal relaxivity  $r_1$  and transverse relaxivity  $r_2$ ) were obtained by normalizing the relaxation enhancement of water protons to a millimolar solution of  $Fe_3O_4$ .

## 3 Results and discussions

Figure 1 shows the micrographs of  $NPs_{ww}$  (Fig. 1a),  $NPs_{wp}$  (Fig. 1c) and  $NPs_{pp}$  (Fig. 1e). For the three samples, the shape of SPI-ONs is spherical. To obtain the mean diameter, a fit by a gaussian function is carried out. The mean diameter is equal to  $2.67 \pm 0.76$  nm,  $3.00 \pm 0.94$  nm and  $3.19 \pm 1.20$  nm for  $NPs_{ww}$ ,  $NPs_{wp}$  and  $NPs_{pp}$  respectively thanks to the size distribution of each samples, obtained with a lower magnification (Fig. 1b, Fig. 1d and Fig. 1f). The size distribution obtained with the NPs synthesised and dispersed in water is narrower than for the synthesis or redispersion in physiological serum: the presence of NaCl in physiological serum increases the mean diameter. In addition, with the physiological serum, a little aggregation of NPs appears due to the presence of NaCl. Indeed, a NaCl matrix encompasses SPI-ONs. This matrix is weak when SPI-ONs are just dispersed in physiological serum after synthesis in water (Fig. 1c) and it is more important when the synthesis and the dispersion are in this serum (Fig 1e): the size distribution is so more important in NaCl solution that in ultra-pure water.

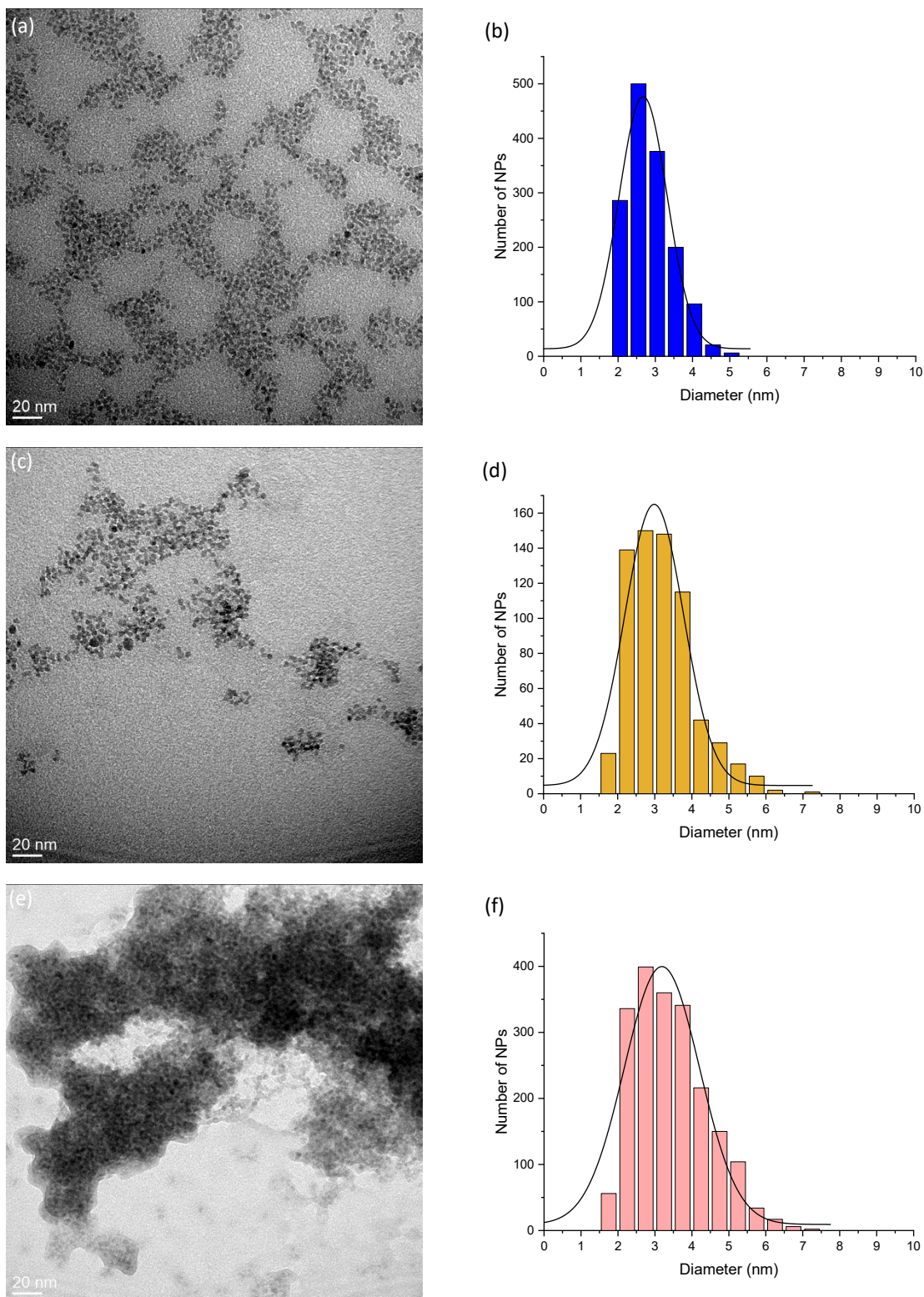


Fig 1: TEM images of  $NPs_{ww}$  (a),  $NPs_{wp}$  (c) and  $NPs_{pp}$  (e) with their size distribution histograms respectively in (b), (d) and (f). The black curve on each histogram represents a fit by a gaussian function.

To confirm this hypothesis, a DLS measurement is carried out. For that, the solution of each NPs was analysed to determine the hydrodynamic diameter as well as the stability of NPs (Fig 2). Indeed, the hydrodynamic diameter is the diameter of the inorganic core increased by the thickness of the organic layer and the solvation sphere. The DLS measurements are expressed in number to be compared with the obtained TEM results. The mean hydrodynamic diameter of samples (determined by a log-normal fit) is equal to  $7 \pm 2$  nm for  $NPs_{ww}$ ,  $11 \pm 3$  nm for  $NPs_{wp}$  and  $10 \pm 2$  nm for  $NPs_{pp}$ .

these values are higher than the diameter obtained by TEM measurements confirming the presence of an organic layer. In addition, as shown in the TEM micrographs of  $\text{NPs}_{\text{wp}}$  and  $\text{NPs}_{\text{pp}}$  (figure 1.c and 1.e), an aggregation of SPIONs is present and increases the value of the hydrodynamic diameter: it is the reason that the hydrodynamic diameter of  $\text{NPs}_{\text{wp}}$  and  $\text{NPs}_{\text{pp}}$  are higher than the hydrodynamic diameter of  $\text{NPs}_{\text{ww}}$ . Finally, the presence of the NaCl matrix can increase a little the mean hydrodynamic diameter in agreement with TEM observations. To confirm the presence of this NaCl matrix, XRD measurements are carried out.

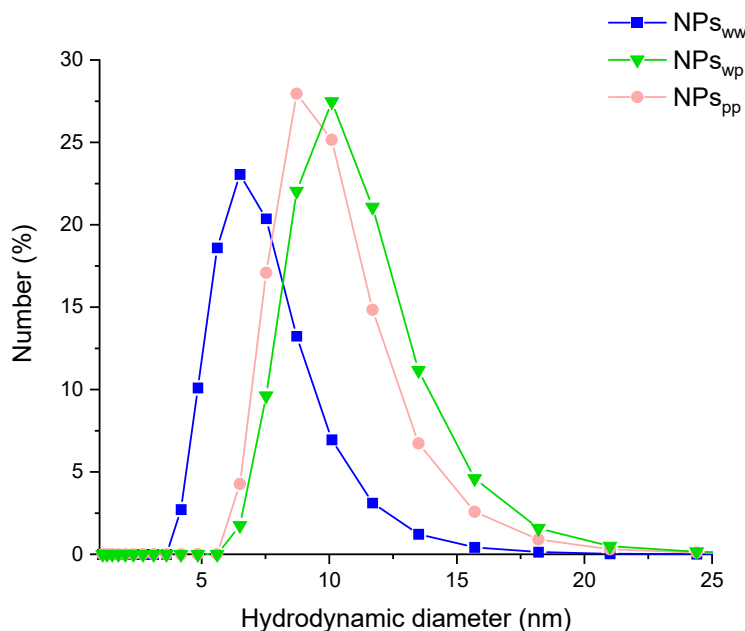


Fig 2: DLS measurements of  $\text{NPs}_{\text{ww}}$  (blue),  $\text{NPs}_{\text{wp}}$  (green) and  $\text{NPs}_{\text{pp}}$  (pink) as function of number of NPs.

Then, a XRD measurement is performed to describe the inorganic core and precisely the crystallographic structure (Fig. 3). Indeed, it exists two types of SPIONs which are magnetite  $\text{Fe}_3\text{O}_4$  and maghemite  $\gamma\text{-Fe}_2\text{O}_3$ . These two iron oxide compositions crystallize in the same inverse spinel structure ( $F_{d\bar{3}m}$ ). The lattice parameter is equal to 8.385 Å and 8.354 Å for magnetite and maghemite respectively. XRD patterns of each samples are compared with a reference pattern of magnetite (COD: 9005836). For the three samples, the main diffraction peaks of magnetite, i.e. (200), (311), (400), (511) and (440), are present.

The lattice parameter is calculated for each sample thanks to these main peaks and it is equal to 8.38 Å, 8.36 Å and 8.37 Å for  $\text{NPs}_{\text{ww}}$ ,  $\text{NPs}_{\text{wp}}$  and  $\text{NPs}_{\text{pp}}$  respectively. These calculated lattice parameters are between those of magnetite and maghemite: the synthesized NPs for this study correspond to  $\text{Fe}_{3-\delta}\text{O}_4$  sub-stoichiometric magnetite with  $\delta$  the stoichiometric deviation. Using XRD patterns, the crystallite size can be calculated thanks to the Debye-Scherrer equation which is  $t = (k\lambda)/(\beta\cos\theta)$  where  $t$  is the size of the crystallite,  $\lambda$  the wavelength of the X-ray radiation,  $\beta$  the FWHM of the main peak with a correction and  $\theta$  the Bragg angle. The crystallite size is similar to the diameter obtained with the TEM for the three sample: 3.3 nm, 3.7 nm and 3.6 nm respectively for  $\text{NPs}_{\text{ww}}$ ,  $\text{NPs}_{\text{wp}}$  and  $\text{NPs}_{\text{pp}}$ .

In addition, for  $\text{NPs}_{\text{wp}}$  and  $\text{NPs}_{\text{pp}}$ , several peaks are present and correspond to a NaCl phase (COD: 231042) in agreement with the interpretation of the matrix and slight aggregation observed on TEM micrographs (Fig. 1c and Fig. 1e) as resulting from the use of physiological serum containing NaCl. To confirm the presence or the absence of NaCl in each sample as function of aqueous solvent and to determine the oxidation state of iron in the inorganic core, Raman spectroscopy measurements are carried out.

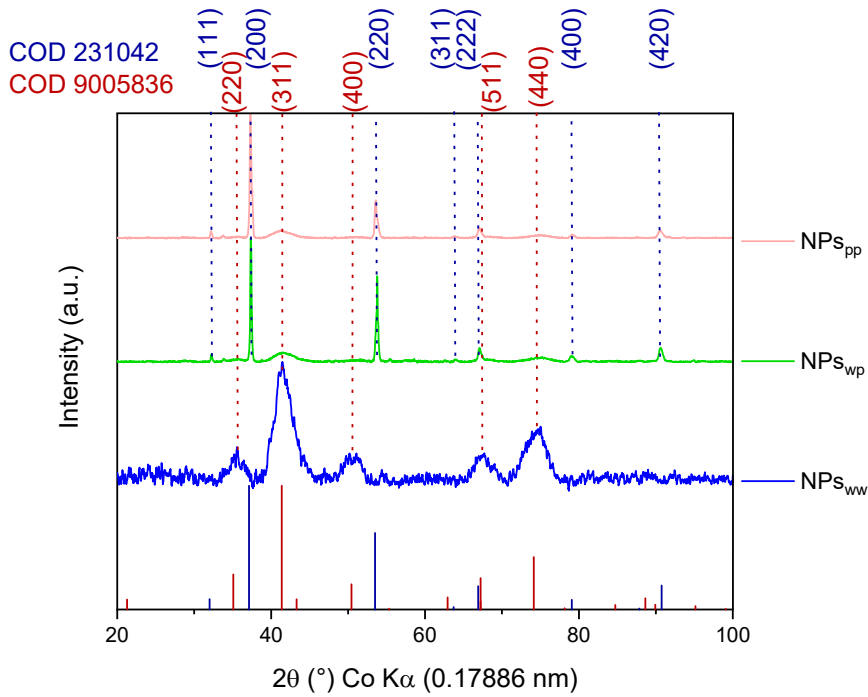


Fig 3: XRD patterns of  $\text{NPs}_{\text{ww}}$  (blue),  $\text{NPs}_{\text{wp}}$  (green) and  $\text{NPs}_{\text{pp}}$  (pink) with a comparison of reference patterns of magnetite  $\text{Fe}_3\text{O}_4$  (COD 9005836) and sodium chloride  $\text{NaCl}$  (COD 231042).

The Raman spectra are illustrated on Fig. 4. For the three samples, we observe the vibrational modes of  $\text{Fe}_3\text{O}_4$ :  $E_g$  at  $300\text{ cm}^{-1}$ ,  $T_{2g}$  at  $540\text{ cm}^{-1}$  and  $A_{1g}$  at  $670\text{ cm}^{-1}$  [42]. This last mode is characteristic of the oxidation state of the iron oxide: a narrow band is representative of magnetite and a large band from  $660$  to  $720\text{ cm}^{-1}$  with a split of this mode into two components is representative of maghemite. For the three samples, we can see an enlargement with the appearance of a shoulder for the  $A_{1g}$  mode by comparison with the magnetite spectrum. This observation implying an oxidation of the nanoparticles without a complete split characteristic of the unique presence of maghemite confirm the synthesis of  $\text{Fe}_{3-\delta}\text{O}_4$  sub-stoichiometric magnetite for all samples as determined by XRD measurements. In addition, for  $\text{NPs}_{\text{wp}}$  and  $\text{NPs}_{\text{pp}}$ , the presence of  $\text{NaCl}$  is confirmed with the Raman spectroscopy. Indeed, several bands are present at  $425\text{ cm}^{-1}$ ,  $1257\text{ cm}^{-1}$ ,  $1323\text{ cm}^{-1}$ ,  $1385\text{ cm}^{-1}$  and  $1660\text{ cm}^{-1}$  and are similar with the bands on a  $\text{NaCl}$  spectrum (Fig.4).



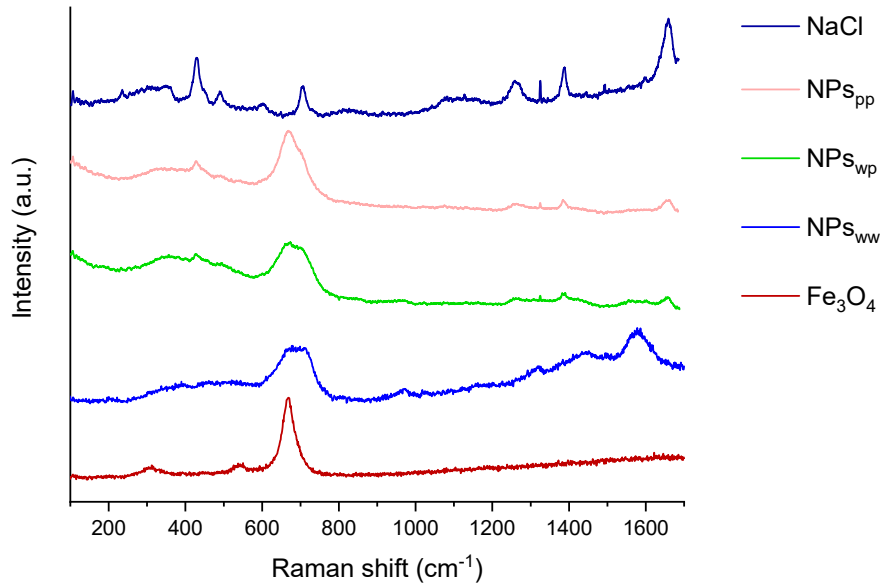


Fig. 4: Raman spectra of  $\text{NPs}_{\text{ww}}$  (blue),  $\text{NPs}_{\text{wp}}$  (green) and  $\text{NPs}_{\text{pp}}$  (pink) obtained with a laser at 633 nm at room temperature compared to a magnetite reference  $\text{Fe}_3\text{O}_4$  and a sodium chloride reference NaCl.

Then, the magnetic properties of each sample are analysed to determine the magnetic state and the saturation magnetization (Fig. 5). For this goal, the evolution of the magnetic moment  $M$  ( $\text{emu.g}^{-1}$ ) in function of magnetic field  $H$  (Oe) is analysed at 300K and at 5K. Indeed, at room temperature (Fig. 5a), the superparamagnetic state can be determined thanks to the presence of a hysteresis or not: without hysteresis, NPs are in a superparamagnetic state; with hysteresis, NPs are in a permanent magnetic state such as ferrimagnetic, ferromagnetic or antiferromagnetic. For the three samples studied here, the absence of hysteresis indicates the superparamagnetic state. With this curve, the magnetization saturation can be determined: it is equal to  $55 \text{ emu.g}^{-1}$ ,  $29 \text{ emu.g}^{-1}$  and  $31 \text{ emu.g}^{-1}$  for  $\text{NPs}_{\text{ww}}$ ,  $\text{NPs}_{\text{wp}}$  and  $\text{NPs}_{\text{pp}}$  respectively. The presence of NaCl in  $\text{NPs}_{\text{wp}}$  and in  $\text{NPs}_{\text{pp}}$  decreases the magnetization saturation because NaCl is a diamagnetic compound: iron oxide nanoparticles are surrounded by a NaCl matrix.

To confirm the superparamagnetic state, a magnetic measurement at 5K is carried out (Fig. 5b). At this temperature, the magnetic moment on iron oxide is in a blocked state so the magnetic behaviour is similar to a cooperative magnetism thus generating a hysteresis in the magnetic curves (Fig. 5c). The magnetization saturation obtained at 5K is higher to the magnetization saturation at 300K due to the blocked state of the magnetic moment: it is equal to  $78 \text{ emu.g}^{-1}$ ,  $38 \text{ emu.g}^{-1}$  and  $41 \text{ emu.g}^{-1}$  for  $\text{NPs}_{\text{ww}}$ ,  $\text{NPs}_{\text{wp}}$  and  $\text{NPs}_{\text{pp}}$  respectively.

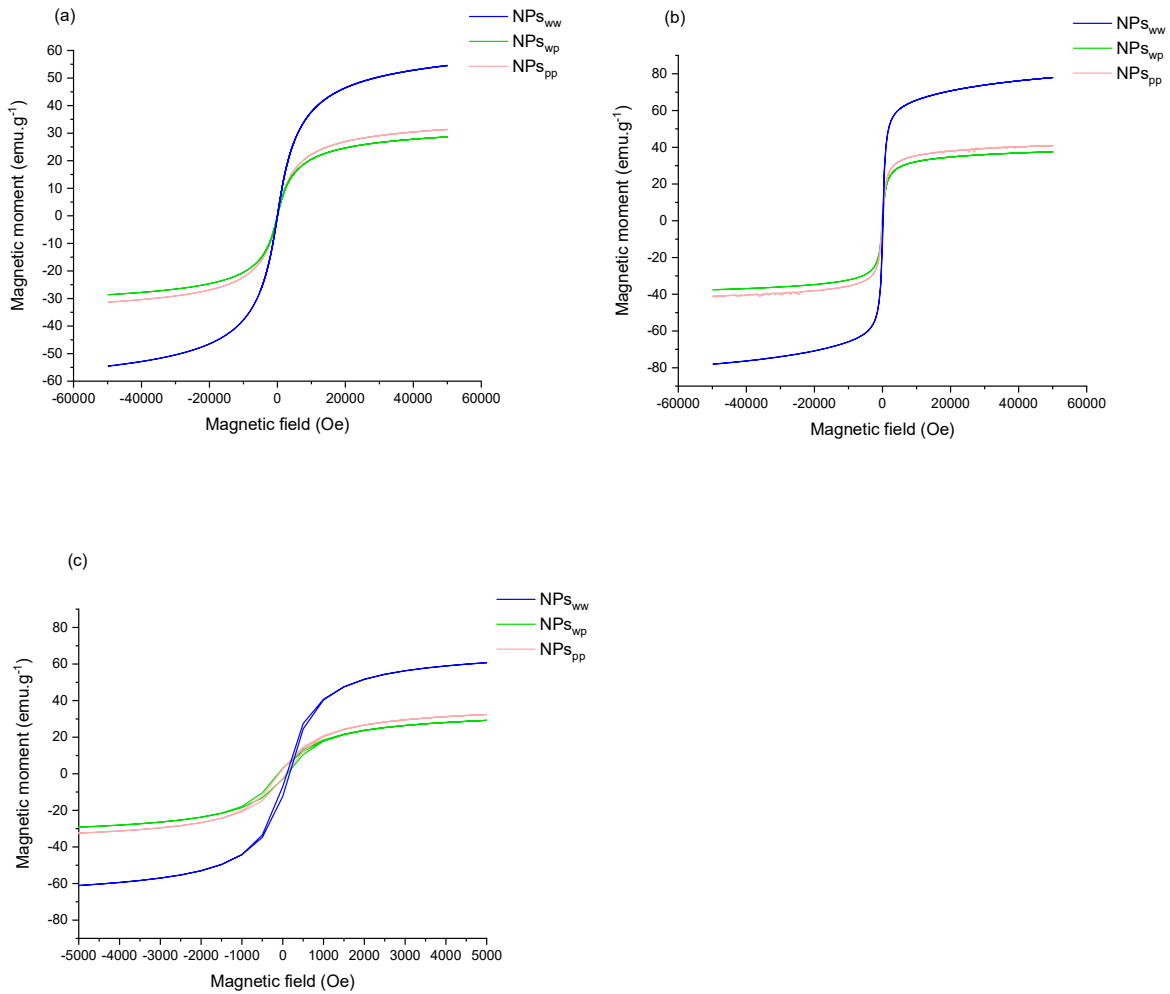


Fig 5: Magnetic moment (emu.g<sup>-1</sup>) as function of magnetic field (Oe) for NPs<sub>ww</sub> (blue), NPs<sub>wp</sub> (green) and NPs<sub>pp</sub> (pink) at 300K (a), at 5K (b) and a zoom at 5K (c).

To complete magnetic characterizations, a ZFC-FC (Zero Field Cooled – Field Cooled) measurement is carried out to determine the blocking temperature  $T_B$ : this temperature is the transition between the superparamagnetic state and the blocked state (Fig. 6). Several methods exist to determine exactly the value of  $T_B$  with a ZFC-FC curve [43]. The most used is an assimilation to the maximum of the ZFC curve (it is the curve from 5K to 300K). For each sample, the determined  $T_B$  is 14K, 25K and 21K for NPs<sub>ww</sub>, NPs<sub>wp</sub> and NPs<sub>pp</sub> respectively: all samples present a superparamagnetic state at room temperature. In addition, the ZFC-FC curves can be considered as a  $T_B$  distribution. For an aggregation of NPs or a larger size distribution, the curve will be larger while for a narrow size distribution of NPs, the curve will be narrower. In agreement, the ZFC curve is narrow for NPs<sub>ww</sub> and larger for NPs<sub>wp</sub> and NPs<sub>pp</sub>. For these two samples, the distribution increase is due to the presence of the NaCl matrix. Indeed, this matrix encapsulates iron oxide nanoparticles thus creating a set of nanoparticles: this set has a higher size compared to a single nanoparticle according to a magnetic point of view with a collective behaviour.

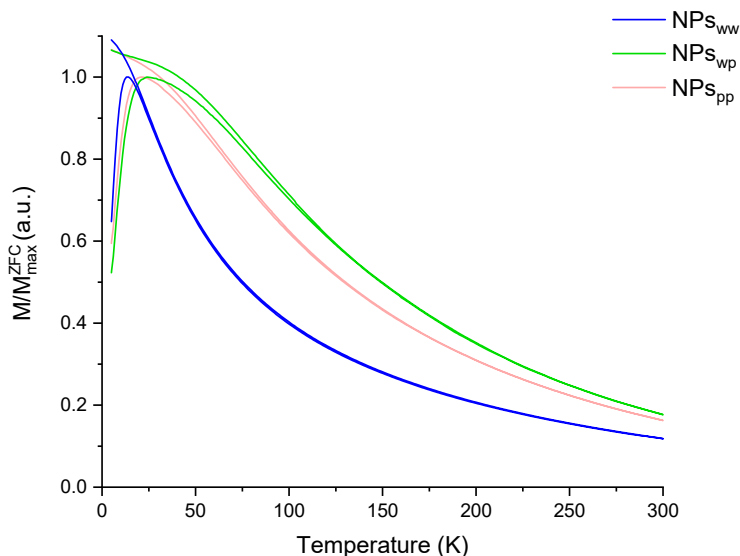


Fig 6: Magnetic moment as function the temperature measured under a magnetic field (200 Oe) of NPs<sub>ww</sub> (blue), NPs<sub>wp</sub> (green) and NPs<sub>pp</sub> (pink).

Finally, for the application of SPIONs as contrast agents in MRI, the value of relaxivity  $r_i$  ( $s^{-1} \cdot \text{mmol}^{-1} \cdot \text{L}$ ) has to be evaluated. This is done by measuring the relaxation rate  $R_i$  ( $i = 1; 2$ ) as a function of SPIONs concentration (at  $37^\circ\text{C}$  and  $1.41\text{T}$ , Fig. 7). Indeed, the paramagnetic contribution to relaxation is linearly proportional to the concentration of CA according to the equation  $R_i = r_i \cdot C + (1/T_0)$  where  $C$  is the concentration of SPIONs (mM) and  $T_0$  is the relaxation time of the aqueous solution without paramagnetic agent. The parameter  $r_i$  is called proton relaxivity and is given in  $s^{-1} \cdot \text{mM}^{-1}$ . Here both types of relaxivities, i.e. longitudinal  $r_1$  and transverse  $r_2$ , are obtained from the linear fitting of data in Fig.7 in order to evaluate the efficiency of SPIONs to act as a contrast agent. Concerning longitudinal relaxation, the relaxivity  $r_1$  is  $17 s^{-1} \cdot \text{mmol}^{-1} \cdot \text{L}$ ,  $12 s^{-1} \cdot \text{mmol}^{-1} \cdot \text{L}$  and  $18 s^{-1} \cdot \text{mmol}^{-1} \cdot \text{L}$  for NPs<sub>ww</sub>, NPs<sub>wp</sub> and NPs<sub>pp</sub> respectively. The relaxivity of NPs<sub>wp</sub> is slightly lower than equivalent relaxivities of NPs<sub>ww</sub> and NPs<sub>pp</sub>. However, for the transverse relaxivity  $r_2$ , which is known to be the relevant parameter for superparamagnetic iron oxide nanoparticles used as negative contrast agent [8,9], NPs<sub>wp</sub> has a higher value than the others. Indeed, the values are  $69 s^{-1} \cdot \text{mmol}^{-1} \cdot \text{L}$ ,  $44 s^{-1} \cdot \text{mmol}^{-1} \cdot \text{L}$  and  $51 s^{-1} \cdot \text{mmol}^{-1} \cdot \text{L}$  for NPs<sub>wp</sub>, NPs<sub>ww</sub> and NPs<sub>pp</sub> respectively. Compared to a commercial contrast agent (Endorem®), these values of transverse relaxivity are lower (for Endorem®,  $r_1$  is between  $10$  to  $24 s^{-1} \cdot \text{mmol}^{-1} \cdot \text{L}$  and  $r_2$  is between  $100$  to  $158 s^{-1} \cdot \text{mmol}^{-1} \cdot \text{L}$  [44–46]) but the ratio between  $r_2$  and  $r_1$  is similar. This ratio is a good indicator to determine if a contrast agent is a good candidate for MRI: if this ratio is higher to 2, NPs will be good candidate for MRI [47]. For the Endorem®, the ratio is between 4 and 15 according to the different authors. This ratio is equal to 2.6, 5.8 and 2.8 for NPs<sub>ww</sub>, NPs<sub>wp</sub> and NPs<sub>pp</sub> respectively: all samples can be good candidates for MRI, particularly NPs<sub>wp</sub> with a ratio of 5.8 similar to Endorem®.

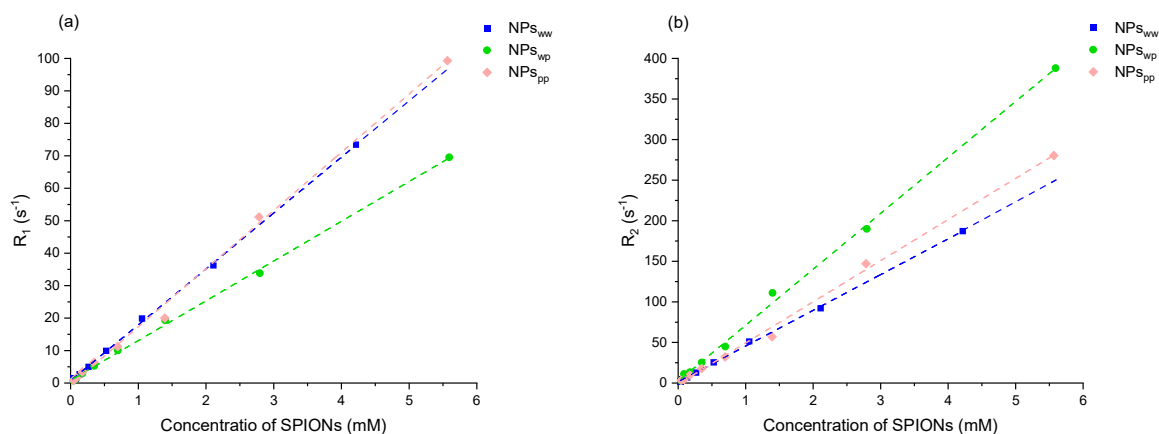


Fig 7: Longitudinal  $R_1$  (a) and transverse  $R_2$  (b) relaxation rate (in  $s^{-1}$ ) as a function of SPIONs concentration (mM) at 60 MHz and 37°C for  $NPs_{ww}$  (blue),  $NPs_{wp}$  (green) and  $NPs_{pp}$  (pink). Dashed lines represent the linear regression done for evaluating the relaxivity  $r_{i=1,2}$

## 4 Conclusion

In summary, thanks to the microwave synthesis, superparamagnetic iron oxide nanoparticles can be synthesised with a small diameter, a good monodispersity and stability in an aqueous solution. These nanoparticles can be used for the biomedical applications with a dispersion in ultra-pure water and in physiological conditions. In this work, for the first time, this synthesis method of SPIONs is performed in ultra-pure water with a validate redispersion in physiological serum (containing 0.9g of NaCl per 100 mL of ultra-pure water) and a direct synthesis in physiological serum is also realised. The nanoparticles obtained by these different conditions offer a small diameter and a colloidal stability thanks to the microwave use and the introduction of an organic layer (a citrate layer) as surfactant during an one-step synthesis. In addition, the inorganic core is a sub-stoichiometric iron oxide ( $Fe_{3-x}O_4$ ) with a good crystallinity and a superparamagnetic state at room temperature. Finally, relaxivity measurements are carried out to conclude that these SPIONs are good candidates for MRI. In particular for the SPIONs synthesised in ultra-pure water and redispersed in physiological serum, the ratio of relaxivity ( $r_2/r_1$ ) is similar to a ratio from a commercial contrast agent (Endorem®).

**Acknowledgments:** We would like to acknowledge the 3M, X-Gamma, Optic Lasers and Magnetism Competence Centers of Institute Jean Lamour for assistance in TEM,

This work was supported by the « SONOMA » project co-funded by FEDER-FSE Lorraine et Massif des Vosges 2014-2020, a European Union Program.

The authors would like to thank the ORION program for its contribution to the funding of LVC's research internship. This work has benefited from a government grant managed by the Agence Nationale de la Recherche with the reference ANR-20-SFRI-0009.

## 5 Reference

1. J. Peng, W. Zhang, L. Chen, T. Wu, M. Zheng, H. Dong, H. Hu, Y. Xiao, Y. Liu, Y. Liang, *Chemical Engineering Journal*, 404 (2021) 126461–126468.
2. R. Ortega-Villar, L. Lizárraga-Mendiola, C. Coronel-Olivares, L.D. López-León, C.A. Bigurra-Alzati, G.A. Vázquez-Rodríguez, *Journal of Environmental Management*, 242 (2019) 487–495.
3. K. Niemirowicz, K. Markiewicz, A. Wilczewska, H. Car, *Advances in Medical Sciences*, 57 (2012) 196–207.

4. S. Mornet, S. Vasseur, F. Grasset, E. Duguet, *J. Mater. Chem.*, 14 (2004) 2161–2175.
5. L.L. Israel, A. Galstyan, E. Holler, J.Y. Ljubimova, *Journal of Controlled Release*, 320 (2020) 45–62.
6. G. Wang, X. Zhang, A. Skallberg, Y. Liu, Z. Hu, X. Mei, K. Uvdal, *Nanoscale*, 6 (2014) 2953–2163.
7. R. Kumar, M. Nayak, G.C. Sahoo, K. Pandey, M.C. Sarkar, Y. Ansari, V.N.R. Das, R.K. Topno, Bhawna, M. Madhukar, P. Das, *Journal of Infection and Chemotherapy*, 25 (2019) 325–329.
8. M.-A. Fortin, C.S.S.R. Kumar (Ed.), *Magnetic Characterization Techniques for Nanomaterials*, Springer Berlin Heidelberg, (2017) Berlin, Heidelberg, 511–555.
9. J. Ward, *Radiography*, 13 (2007) e54–e72.
10. F. Reyes-Ortega, Á. Delgado, G. Iglesias, *Nanomaterials*, 11 (2021) 627–639.
11. Z.E. Gahrouei, M. Imani, M. Soltani, A. Shafyei, *Adv. Nat. Sci. Nanosci. Nanotechnol.*, 11 (2020) 025001–025008.
12. F. Soetaert, P. Korangath, D. Serantes, S. Fiering, R. Ivkov, *Advanced Drug Delivery Reviews*, 163–164 (2020) 65–83.
13. S. Tong, H. Zhu, G. Bao, *Materials Today*, 31 (2019) 86–99.
14. J. Gouyau, R.E. Duval, A. Boudier, E. Lamouroux, *IJMS*, 22 (2021) 1905–1918.
15. W. Xiaoming, G. Shiwei, L. Zhiqian, X. Xueyang, G. Lei, L. Qiang, Z. Hu, G. Qiyong, L. Kui, *Applied Materials Today*, 17 (2019) 92–103.
16. R. Gramiak, P.M. Shah, *Invest Radiol* (1968) 356–366.
17. T.J. Clough, L. Jiang, K.-L. Wong, N.J. Long, *Nat Commun*, 10 (2019) 1420–1433.
18. V.F. Cardoso, A. Francesko, C. Ribeiro, M. Bañobre-López, P. Martins, S. Lanceros-Mendez, *Advanced Healthcare Materials*, 7 (2018) 1700845.
19. A. Espinosa, R. Di Corato, J. Kolosnjaj-Tabi, P. Flaud, T. Pellegrino, C. Wilhelm, *ACS Nano*, 10 (2016) 2436–2446.
20. X. Battle, C. Moya, M. Escoda-Torroella, Ò. Iglesias, A.F. Rodríguez, A. Labarta, *Journal of Magnetism and Magnetic Materials*, 543 (2022) 168594.
21. E. Taboada, E. Rodríguez, A. Roig, J. Oró, A. Roch, R.N. Muller, *Langmuir*, 23 (2007) 4583–4588.
22. P. Arévalo, J. Isasi, A.C. Caballero, J.F. Marco, F. Martín-Hernández, *Ceramics International*, 43 (2017) 10333–10340.
23. S. Slimani, C. Meneghini, M. Abdolrahimi, A. Talone, J.P.M. Murillo, G. Barucca, N. Yaacoub, P. Imperatori, E. Illés, M. Smari, E. Dhahri, D. Peddis, *Applied Sciences*, 11 (2021) 5433–5435.
24. K. Petcharoen, A. Sirivat, *Materials Science and Engineering: B*, 177 (2012) 421–427.
25. O.A. Abu-Noqta, A.A. Aziz, A.I. Usman, *Materials Today: Proceedings*, 17 (2019) 1072–1077.
26. S. Nigam, K.C. Barick, D. Bahadur, *Journal of Magnetism and Magnetic Materials*, 323 (2011) 237–243.
27. T. Girardet, A. Cherraj, A. Pinzano, C. Henrionnet, F. Cleymand, S. Fleutot, *Pure and Applied Chemistry*, 93 (2021) 1265–1273.
28. C. Tao, Y. Chen, D. Wang, Y. Cai, Q. Zheng, L. An, J. Lin, Q. Tian, S. Yang, *Nanomaterials*, 9 (2019) 699–711.
29. Ika.O. Wulandari, H. Sulistyarti, A. Safitri, D.J.D.H. Santjojo, A. Sabarudin, *J App Pharm Sci*, 9 (2019) 1–11.
30. M. Anbarasu, M. Anandan, E. Chinnasamy, V. Gopinath, K. Balamurugan, *Spectrochimica Acta Part A: Molecular and Biomolecular Spectroscopy*, 135 (2015) 536–539.
31. H. Kahil, A. Faramawy, H. El-Sayed, A. Abdel-Sattar, *Crystals*, 11 (2021) 1153–1168.
32. T. Lu, J. Wang, J. Yin, A. Wang, X. Wang, T. Zhang, *Colloids and Surfaces A: Physicochemical and Engineering Aspects*, 436 (2013) 675–683.
33. A.G. Roca, L. Gutiérrez, H. Gavilán, M.E. Fortes Brollo, S. Veintemillas-Verdaguer, M. del P. Morales, *Advanced Drug Delivery Reviews*, 138 (2019) 68–104.
34. X. Guo, W. Wang, Y. Yang, Q. Tian, *CrystEngComm*, 18 (2016) 9033–9041.
35. O. Bixner, A. Lassenberger, D. Baurecht, E. Reimhult, *Langmuir*, 31 (2015) 9198–9204.
36. F. Crippa, L. Rodriguez-Lorenzo, X. Hua, B. Goris, S. Bals, J.S. Garitaonandia, S. Balog, D. Burnand, A.M. Hirt, L. Haeni, M. Lattuada, B. Rothen-Rutishauser, A. Petri-Fink, *ACS Appl. Nano Mater.*, 2 (2019) 4462–4470.
37. E. Aivazoglou, E. Metaxa, E. Hristoforou, *AIP Advances*, 8 (2018) 048201–048214.
38. I. Fernández-Barahona, M. Muñoz-Hernando, F. Herranz, *Molecules*, 24 (2019) 1224–1258.
39. Y.-J. Liang, Y. Zhang, Z. Guo, J. Xie, T. Bai, J. Zou, N. Gu, *Chem. Eur. J.*, 22 (2016) 11807–11815.
40. P. Venturini, S. Fleutot, F. Cleymand, T. Hauet, J. Dupin, J. Ghanbaja, H. Martinez, J. Robin, V. Lapinte, *ChemistrySelect*, 3 (2018) 11898–11901.
41. M.D. Abràmoff, P.J. Magalhães, S.J. Ram, *Biophotonics International*, 36–32, 2004.
42. M. Hanesch, *Geophysical Journal International*, 177 (2009) 941–948.
43. I.J. Bruvera, P. Mendoza Zélis, M. Pilar Calatayud, G.F. Goya, F.H. Sánchez, *Journal of Applied Physics*, 118 (2015) 184304–184310.
44. N. Ohannesian, C.T. De Leo, K.S. Martirosyan, *Materials Today: Proceedings*, 13 (2019) 397–403.
45. M. Geppert, M. Himly, *Front. Immunol.*, 12 (2021) 688927–688934.
46. A.M. Predescu, E. Matei, A.C. Berbecaru, C. Pantilimon, C. Drăgan, R. Vidu, C. Predescu, V. Kuncser, *R. Soc. Open Sci.*, 5 (2018) 171525–171535.
47. Y. Gossuin, P. Gillis, A. Hocq, Q.L. Vuong, A. Roch, *WIREs Nanomed Nanobiotechnol*, 1 (2009) 299–310.